Demonstration of Linear Covariance Analysis Techniques to Evaluate Entry Descent and Landing Guidance Algorithms, Vehicle Configurations, Analysis Techniques, and Trajectory Profiles

William E. Brandenburg*, James W. Williams†
University of Illinois at Urbana-Champaign, Urbana, Illinois, 61801, USA

David C. Woffinden‡
NASA Johnson Space Center, Houston, Texas, 77058, USA

Zachary R Putnam§
University of Illinois at Urbana-Champaign, Urbana, Illinois, 61801, USA

Linear covariance analysis techniques have been previously developed to analyze closed-loop entry, descent, and landing (EDL) scenarios and the initial validation efforts are underway confirming the generated GN&C system performance results. Given both the theoretical foundation and previous conceptual demonstration, this work begins to flex the potential of linear covariance analysis for atmospheric flight and highlight its versatility and reliability by evaluating multiple entry guidance algorithms, vehicle configurations, trajectory profiles, environment conditions, and analysis techniques for a variety of trade studies. To demonstrate the benefit linear covariance analysis can provide in producing rapid yet accurate performance data, two entry profiles are adopted including the NASA Mars Science Laboratory (MSL) and Exploration Flight Test-1 (EFT-1) while utilizing two different guidance algorithms, the Apollo Final Phase (AFP) and the Fully Numeric Predictor-Corrector Entry Guidance (FNPEG) with different navigation sensor suites in a 6 degree-of-freedom (6-DOF) simulation environment. Results are shown using both linear covariance and Monte Carlo analysis techniques to highlight the consistency between the two methodologies and continue the validation maturation of linear covariance analysis for entry, descent, and landing.

I. Introduction

The Safe and Precise Landing and Integrated Capabilities Evolution (SPLICE) project[1] continues advancing the technology to support exploration missions to Mars and other celestial bodies as mission objectives seek to land mission-critical assets safely and precisely. Part of this effort includes the generation of navigation and sensor requirements for these future entry, descent, and landing (EDL) systems. This often requires the capability to perform extensive trade studies quickly and reliably during the early conceptual design phase. Understanding the sensitivities and key drivers influencing the integrated performance of the guidance, navigation, and control (GN&C) system becomes critical.

Linear covariance analysis (LinCov) is ideally suited to untangle the complex interdependencies between mission objectives, trajectory design, closed-loop GN&C performance, system uncertainties, and vehicle configuration. Although Monte Carlo (MC) simulation techniques are the current standard for uncertainty analysis for EDL missions, they typically require significant computational resources. It has been recently demonstrated, that in a single LinCov simulation run, it can produce similar statistical performance results as running thousands of Monte Carlo runs[2]. The LinCov techniques developed and demonstrated for atmospheric flight that enable rapid closed-loop, guidance, navigation, and control (GNC) performance analysis[3–7] are expanded upon in this research.

Given both the theoretical foundation and previous conceptual demonstration, this work begins to flex the potential of linear covariance analysis for atmospheric flight and highlight its versatility and reliability by evaluating multiple

---

*Undergraduate Research Assistant & NASA JSC Intern, Aerospace Engineering, AIAA Student Member
†Graduate Research Assistant & NASA JSC Intern, Aerospace Engineering, AIAA Student Member
‡GN&C Autonomous Flight Systems Branch, Aeroscience and Flight Mechanics Division, AIAA Professional Member
§Assistant Professor, Aerospace Engineering, AIAA Senior Member

entry guidance algorithms, vehicle configurations, trajectory profiles, environment conditions, and analysis techniques for a variety of trade studies. To demonstrate the benefit linear covariance analysis can provide in producing rapid yet accurate performance data, two entry profiles are adopted including the NASA Exploration Flight Test-1 (EFT-1) and Mars Science Laboratory (MSL) while utilizing two different guidance algorithms, the Apollo Final Phase (AFP) and the Fully Numeric Predictor-Corrector Entry Guidance (FNPEG) with different navigation sensor suites in a 6 degree-of-freedom (6-DOF) simulation environment. Results are shown using both linear covariance and Monte Carlo analysis techniques to highlight the consistency between the two methodologies and continue the validation process of linear covariance analysis for entry, descent, and landing.

The paper is organized as follows where Section II gives an overview of GN&C performance analysis techniques and EDL reference missions. Section III outlines the mathematical models and key analysis input parameters. Section IV provides the closed-loop GN&C performance results from both the Mars and Earth EDL scenarios and highlights key metrics from the various trades, and Section V makes final concluding observations.

II. GN&C Performance Analysis Overview

This section provides an overview of the analysis techniques and performance metrics used to evaluate the entry, descent, and landing scenarios. It also outlines the specific EDL trajectory profiles and concept of operations evaluated in this study along with the models associated with the environment, vehicle configuration, sensors, and guidance algorithms.

A. Analysis Techniques

To analyze a GN&C system, whether using Monte Carlo or linear covariance analysis techniques, there are several key variables of interest that are utilized to characterize the system's integrated performance. As depicted in Figure 1, these variables include the environment dispersions $\delta \mathbf{x}$, the navigation dispersions $\delta \hat{\mathbf{x}}$, the actual navigation error $\delta \mathbf{e}$, and the onboard navigation error $\delta \hat{\mathbf{e}}$.
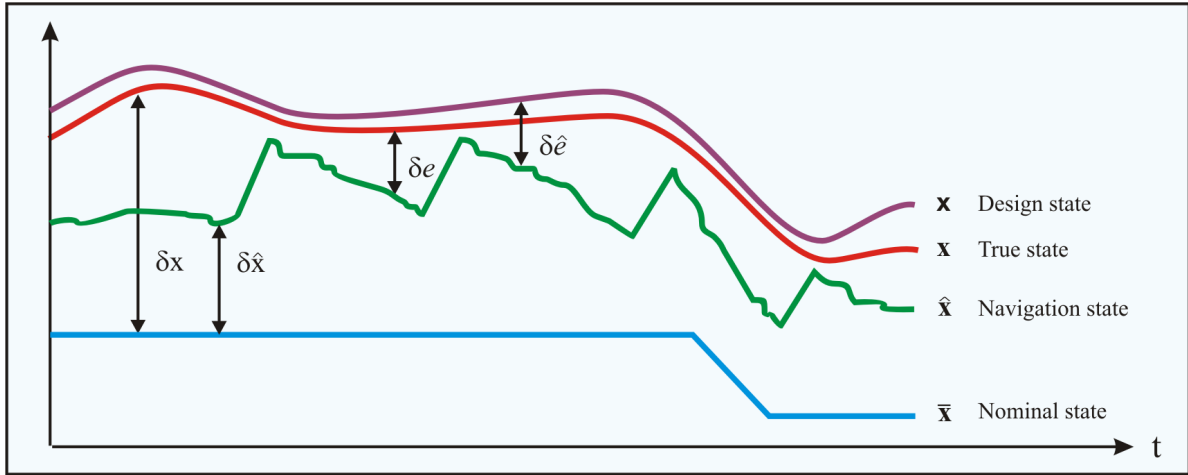

Fig. 1   GN&C performance metric variables.

The true dispersions $\delta \mathbf{x}$ are defined as the difference between the true state $\mathbf{x}$ and the nominal state $\bar{\mathbf{x}}$. The true state $\mathbf{x}$ is an n-dimensional vector that represents the *real world* environment or actual state.

$$\delta \mathbf{x} \overset{\Delta}{=} \mathbf{x} - \bar{\mathbf{x}} \qquad \mathbf{D} = E\left[\delta \mathbf{x} \delta \mathbf{x}^{\mathrm{T}}\right] \qquad (1)$$

The nominal state $\bar{\mathbf{x}}$ is also an n-dimensional vector that represents the desired or reference state. The covariance of the environment dispersions, $\mathbf{D}$, indicates how precisely the system can follow a desired trajectory.

The navigation dispersions $\delta \hat{\mathbf{x}}$ are defined as the difference between the navigation state $\hat{\mathbf{x}}$ and the nominal state $\bar{\mathbf{x}}$. The navigation state is an $\hat{n}$-dimensional vector ($\hat{n} < n$) that represents the filter's estimated state.

$$\delta \hat{\mathbf{x}} \overset{\Delta}{=} \hat{\mathbf{x}} - \hat{\mathbf{N}}_x \bar{\mathbf{x}} \qquad \hat{\mathbf{D}} = E\left[\delta \hat{\mathbf{x}} \delta \hat{\mathbf{x}}^{\mathrm{T}}\right] \qquad (2)$$

The matrix $\hat{\mathbf{N}}_x$ is an $(\hat{n} \times n)$ matrix that maps the estimated state in terms of the true and nominal state. The covariance of the navigation dispersions, $\hat{\mathbf{D}}$, reflect how precisely the onboard system thinks it can follow a prescribed reference trajectory.

The true navigation error $\delta\mathbf{e}$ is the difference between the environment and navigation states. It is also the difference between the environment and the navigation dispersions.

$$\delta\mathbf{e} \overset{\Delta}{=} \hat{\mathbf{N}}_x\mathbf{x} - \hat{\mathbf{x}} = \hat{\mathbf{N}}_x\delta\mathbf{x} - \delta\hat{\mathbf{x}} \qquad\qquad \mathbf{P} = E\left[\delta\mathbf{e}\delta\mathbf{e}^{\mathrm{T}}\right] \qquad\qquad (3)$$

The covariance of the true navigation error, $\mathbf{P}$, quantifies how precisely the onboard navigation system can estimate the actual state.

The onboard navigation error $\delta\hat{\mathbf{e}}$ itself is never computed, but it is used to develop the onboard navigation filter equations. It is defined as the difference between the design state, x, and the navigation state $\hat{\mathbf{x}}$.

$$\delta\hat{\mathbf{e}} \overset{\Delta}{=} \mathrm{x} - \hat{\mathbf{x}} \qquad\qquad \hat{\mathbf{P}} = E\left[\delta\hat{\mathbf{e}}\delta\hat{\mathbf{e}}^{\mathrm{T}}\right] \qquad\qquad (4)$$

The covariance of the onboard navigation error, $\hat{\mathbf{P}}$, quantifies how precisely the onboard navigation system expects it can determine the actual state. The performance of the onboard navigation system is determined by comparing $\hat{\mathbf{P}}$ to the actual navigation performance $\mathbf{P}$. If the *true* states and the *design* states are assumed to be the same, then the true navigation covariance will equal the onboard navigation covariance.

1. Monte Carlo Analysis

The covariances of the true dispersions, navigation dispersions, true navigation error, and the onboard navigation error are ultimately used to analyze and assess the performance of a proposed GN&C system. As illustrated in Figure 2, a common approach to obtain these performance metrics is to use a Monte Carlo simulation, where the sample statistics of hundreds or thousands of runs, N, are used to numerically compute the desired covariance matrices.

$$\mathbf{D} = \frac{1}{N-1}\sum\delta\mathbf{x}\delta\mathbf{x}^{\mathrm{T}} \qquad \hat{\mathbf{D}} = \frac{1}{N-1}\sum\delta\hat{\mathbf{x}}\delta\hat{\mathbf{x}}^{\mathrm{T}} \qquad \mathbf{P} = \frac{1}{N-1}\sum\delta\mathbf{e}\delta\mathbf{e}^{\mathrm{T}} \qquad (5)$$

The onboard navigation error covariance $\hat{\mathbf{P}}$ is the navigation filter covariance for each run.
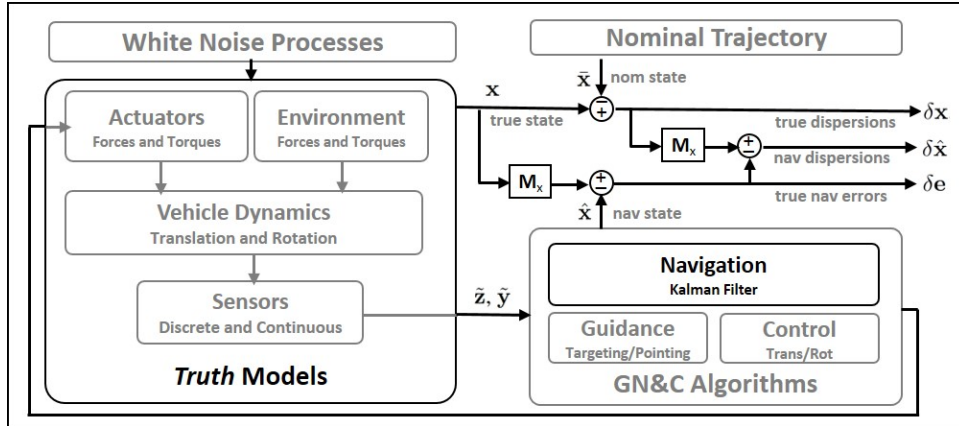

Fig. 2   GN&C performance metrics in a generic Monte Carlo simulation.

2. Linear Covariance Analysis

This same statistical information can be obtained using linear covariance analysis techniques. Linear covariance analysis incorporates the non-linear system dynamics models and GN&C algorithms to generate a nominal reference trajectory $\bar{\mathbf{x}}$ which is then used to propagate, update, and correct the onboard navigation covariance matrix $\hat{\mathbf{P}}$ and an augmented state covariance matrix $\mathbf{C}$,

$$\mathbf{C} = E\left[\delta\mathbf{X}\delta\mathbf{X}^{\mathrm{T}}\right] \qquad\qquad (6)$$

where the augmented state $\delta\mathbf{X}^{\mathrm{T}} = [\delta\mathbf{x}^{\mathrm{T}}\ \delta\hat{\mathbf{x}}^{\mathrm{T}}]$ consists of the true dispersions and the navigation dispersions. Pre- and post-multiplying the augmented state covariance matrix by the following mapping matrices, the covariances for the trajectory dispersions, navigation dispersions, and the navigation error can be obtained.

$$
\begin{aligned}
\mathbf{D} &= [\ \mathbf{I}_{n\times n},\ \mathbf{0}_{n\times\hat{n}}\ ]\,\mathbf{C}\,[\ \mathbf{I}_{n\times n},\ \mathbf{0}_{n\times\hat{n}}\ ]^{\mathrm{T}} \\
\hat{\mathbf{D}} &= [\ \mathbf{0}_{\hat{n}\times n},\ \mathbf{I}_{\hat{n}\times\hat{n}}\ ]\,\mathbf{C}\,[\ \mathbf{0}_{\hat{n}\times n},\ \mathbf{I}_{\hat{n}\times\hat{n}}\ ]^{\mathrm{T}} \\
\mathbf{P} &= [\ \mathbf{I}_{\hat{n}\times n},\ -\mathbf{I}_{\hat{n}\times\hat{n}}\ ]\,\mathbf{C}\,[\ \mathbf{I}_{\hat{n}\times n},\ -\mathbf{I}_{\hat{n}\times\hat{n}}\ ]^{\mathrm{T}}
\end{aligned}
\tag{7}
$$

Both the Monte Carlo and the linear covariance analysis techniques provide a complementary package that can generate the requisite statistical information using different approaches. The true dispersion covariance $\mathbf{D}$ and navigation covariance $\mathbf{P}$ derived in Eqn 5 and Eqn 7 can be compared to confirm expected performance results. Details regarding the fundamental linear covariance framework and equations used to govern the system dynamic models for both the LinCov and Monte Carlo simulation tools for atmospheric entry, descent, and landing were derived previously[4, 5].

B. Reference Missions and EDL Trajectory Profiles

As alluded to earlier and shown in Figure 3, two reference missions are investigated, one at Mars and the other at Earth, to emphasize the variation of atmospheric conditions and impacts of specific celestial bodies on EDL performance analysis using linear covariance techniques. In addition, two different entry guidance algorithms are also simulated to highlight the ability to evaluate the impacts of the selected guidance logic on the integrated closed-loop GN&C performance for potential trade studies. Details regarding these two atmospheric guidance strategies, the Apollo Final Phase (APF) and the Fully Numerical Predictor-Corrector Entry Guidance (FNPPEG), are presented in subsequent sections. The Mars scenario adopted for this study replicates NASA's Mars Science Laboratory (MSL) landing at Gale Crater where the parachute deployment sequence is replaced with a propulsive deceleration for the descent and landing phase. An extensive LinCov validation effort was performed with this profile previously[2] and is used as a *baseline* scenario to contrast variation in performance results. Many of the state parameters used in this study were acquired from Dutta [8]. The Earth EDL scenario utilizes NASA's Exploration Flight Test-1 where the Orion capsule is the entry vehicle. The assumptions for the initial state at entry interface and guidance parameters for the EFT-1 scenario were adopted from Lu [9].

Table 1   MSL Entry Interface State

MSL Entry Interface State	Value
Altitude, km	133.0
Latitude, deg	-3.9186
Longitude, deg	-126.72
Azimuth (inertial), deg	93.2065
Flight-Path Angle (inertial), deg	-15.489
Velocity Magnitude (inertial), km/s	6.08
Angle of Attack, deg	-10
Angle of Bank, deg	-15

Table 2   EFT-1 Entry Interface State

EFT-1 Entry Interface State	Value
Altitude, km	121.9
Latitude, deg	23.61
Longitude, deg	-129.28
Azimuth (inertial), deg	90
Flight-Path Angle (inertial), deg	-6.039
Velocity Magnitude (inertial), km/s	8.928
Angle of Attack, deg	-15
Angle of Bank, deg	-10

Table 3   MSL Touchdown (Gale Crater)

MSL Touchdown (Gale Crater)	Value
Altitude, km	-4.0
Latitude, deg	-4.5895
Longitude, deg	137.4417

Table 4   EFT-1 Touchdown (San Diego, CA)

| EFT-1 Touchdown (San Diego, CA)	Value
Altitude, km	0.0
Latitude, deg	23.61
Longitude, deg	-116.48
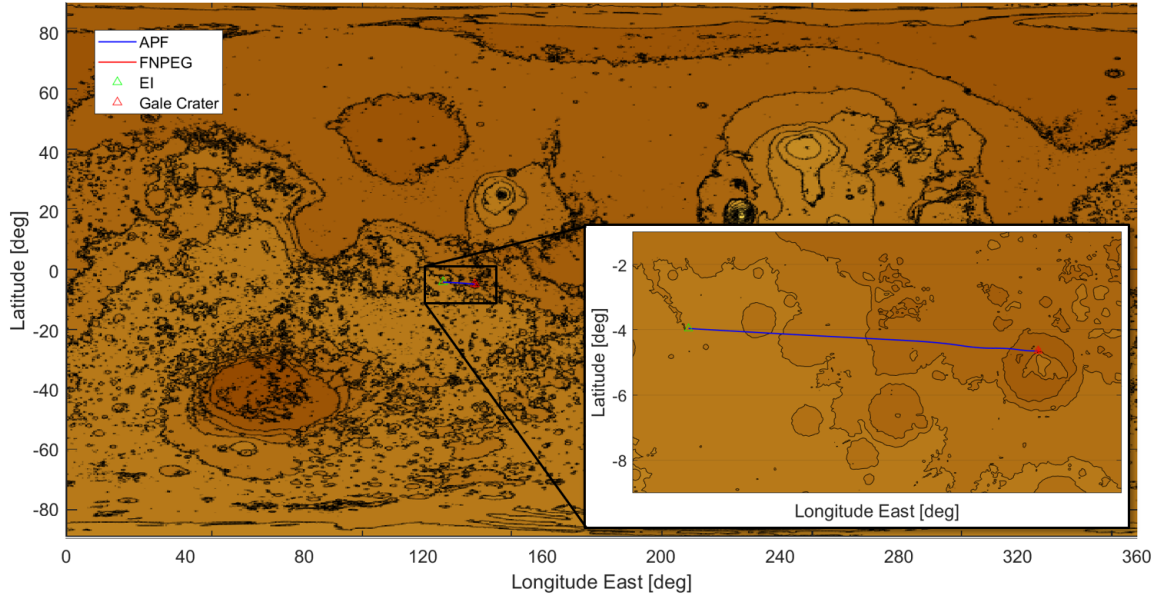
(a) MSL Simulated Ground Tracking Profile Using APF and FNPEG
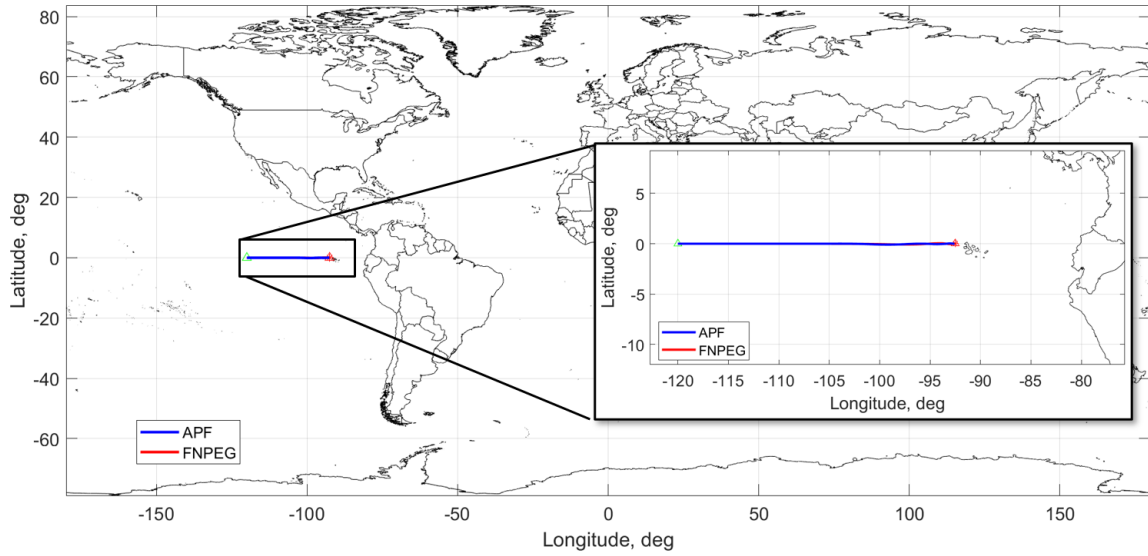
(b) EFT-1 Simulated Ground Tracking Profile Using APF and FNPEG

Fig. 3   Simulated Entry Trajectory for both Apollo Final Phase (APF) and FNPEG
for MSL and EFT-1

Mars Science Laboratory (MSL)   On August 6, 2012, the Mars Science Laboratory, NASA's robotic space probe mission to Mars, successfully landed the Mars Curiosity rover at Gale Crater. At the time, MSL achieved one of the most accurate Martian landing of any known spacecraft touching down within a several kilometers of the designated landing site. A replicated yet slightly modified MSL scenario is simulated as depicted in Figure 3(a) starting at entry interface (EI) and terminating at Mars Gale Crater with the intent to land within 50 meters of the desired location. The specific EI and landing state parameters adopted for this study are summarized in Table 1 and Table 3 respectively. The simulated trajectory profile has four major segments including coast, atmospheric entry, powered descent, and landing as illustrated in Figure 4(a). During the entry phase, both the APF and FNPEG entry guidance algorithms are utilized to control range through bank-angle steering with the actual bank profile shown in Figure 5(a). Results using APF are shown in blue and the bank profile generated with FNPEG is shown in red. The nominal crossrange with respect to
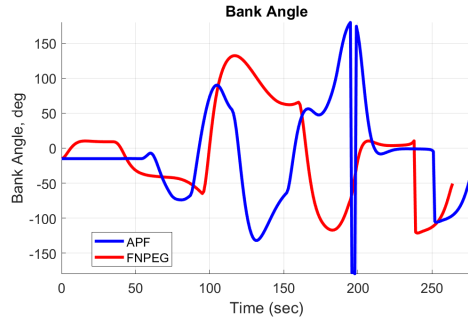
5
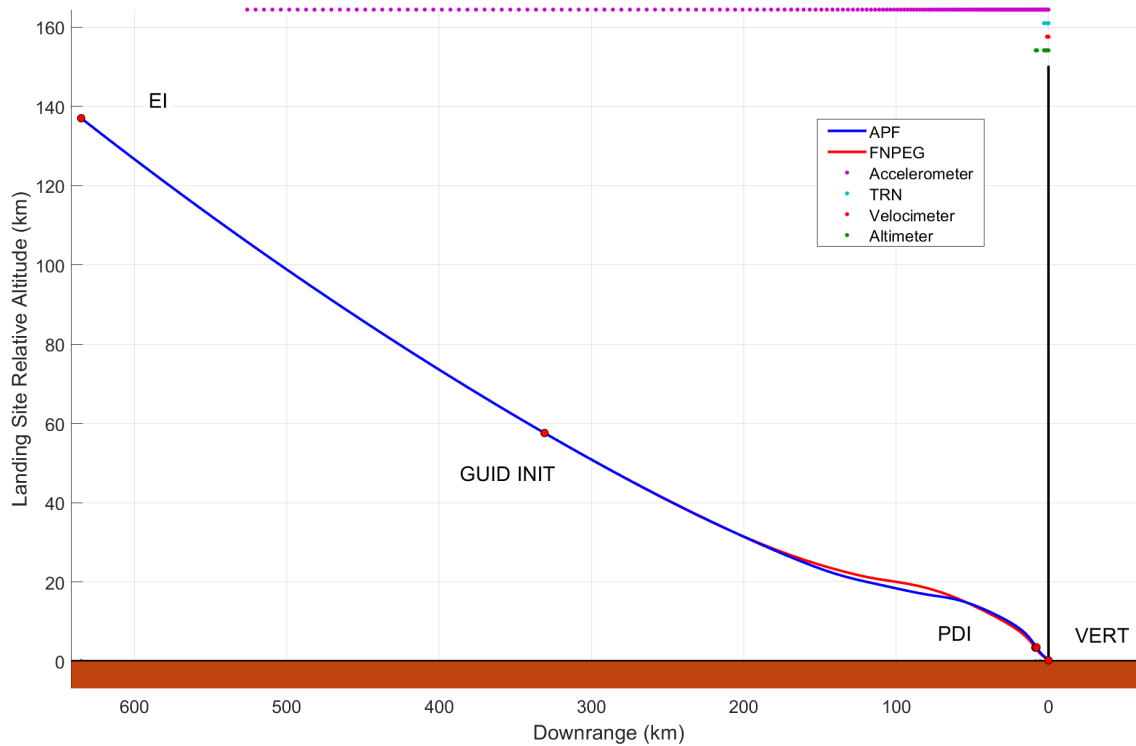
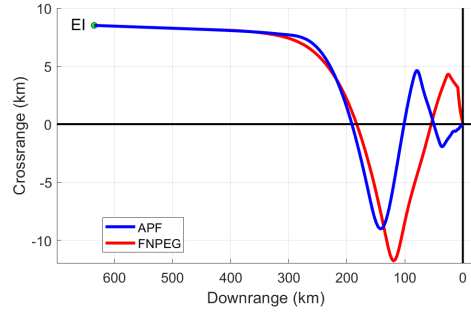(a) MSL Simulated Downrange Versus Altitude Trajectory Profile.
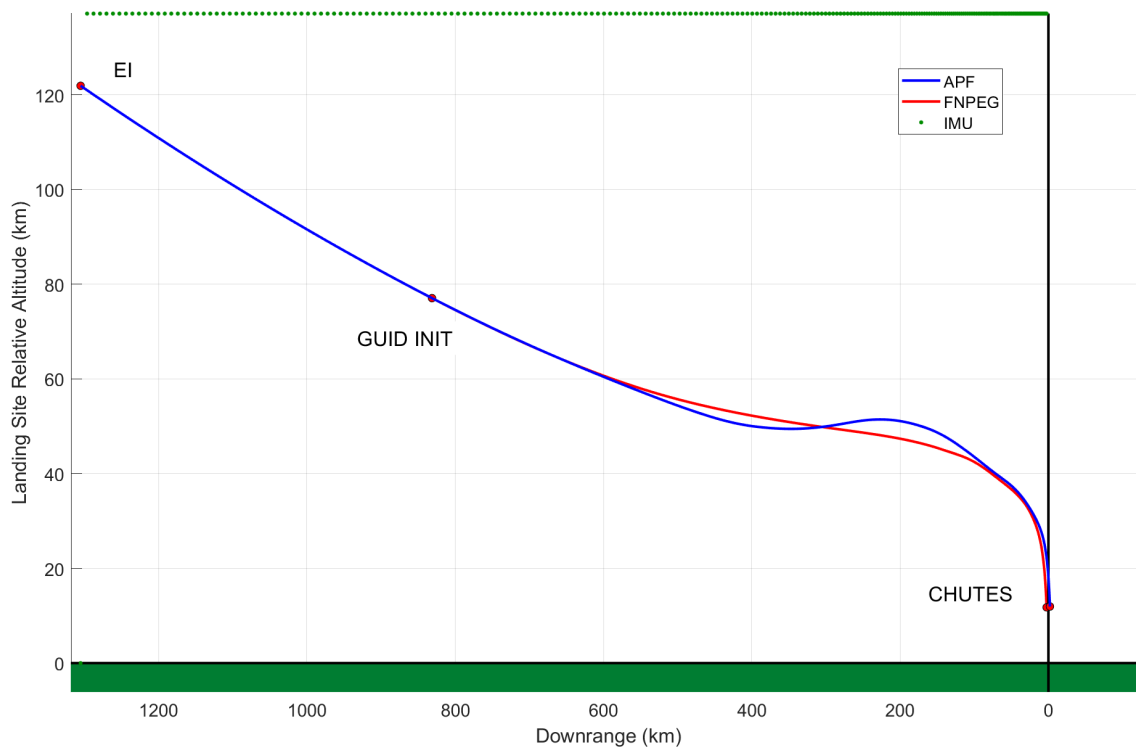
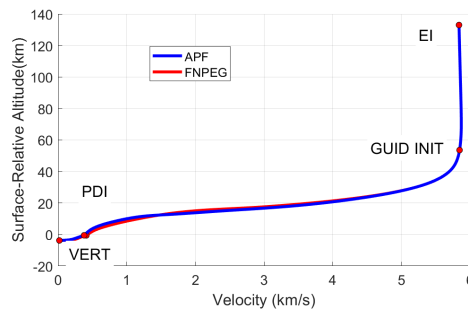(b) EFT-1 Simulated Downrange Versus Altitude Trajectory

Fig. 4   MSL and EFT-1 Entry Profile using both Apollo Final Phase (APF) and FNPEG

(a) MSL Bank Angle Profile

(b) MSL Crossrange Versus Downrange Profile

(c) MSL Altitude Versus Velocity Profile

(d) MSL Aerodynamic Force Profile

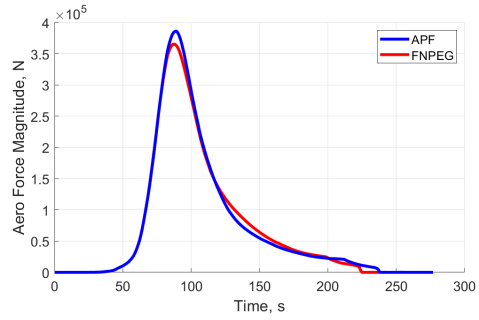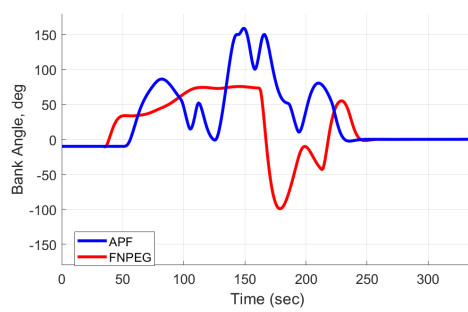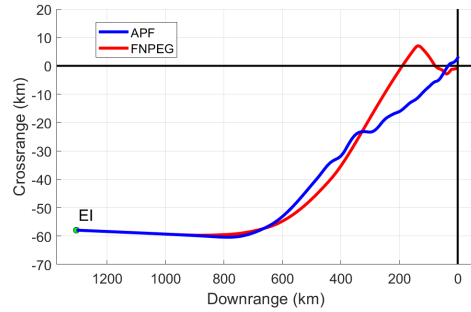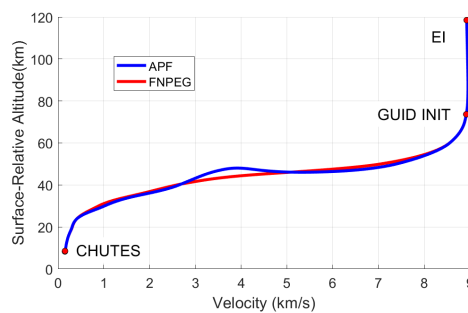**Fig. 5   MSL Simulated Nominal Entry Performance Parameters**
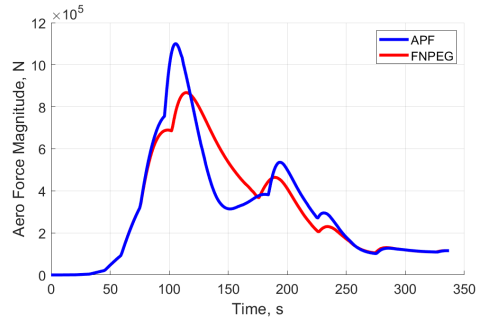

(a) EFT-1 Bank Angle Profile

(b) EFT-1 Crossrange Versus Downrange Profile

(c) EFT-1 Altitude Versus Velocity Profile

(d) EFT-1 Aero Accel Profile

Fig. 6   EFT-1 Simulated Nominal Entry Performance Parameters

7

the lander's velocity magnitude during the entry flight segment is highlighted in Figure 5(b). Both plots highlight the different bank reversals and subsequent cross range profile induced by the selected entry guidance logic. Figure 4(a) gives the MSL altitude profile versus downrange distance which has similar trends between APF and FNPEG. Lastly, Figure 5(d) summarizes the resulting atmospheric forces acting on the vehicle. The current implementation shows the APF generates slightly higher peak atmospheric forces on MSL than FNPEG.

During the coast and atmospheric entry flight phases, only inertial measurements from accelerometers and gyros are available for navigation. When the heatshield and backshell are jettisoned following the entry phase, thrusters and relative sensors are exposed. The relative sensors assumed for this study include an altimeter, velocimeter, and a terrain-relative navigation (TRN) sensor. Following this mass ejection event, the vehicle switches to a linear acceleration fixed time-to-go propulsive descent algorithm[10] to guide the vehicle to a point directly above the landing site with zero horizontal velocity at a target-relative altitude of 200 m and descent rate of 20 m/s. Once the vehicle has reached this point above the landing site, it transitions to a propulsive vertical descent algorithm that linearly decrease the descent rate as a function of altitude such that at touch down the vehicle vertical velocity is 1 m/s.

Orion Exploration Flight Test-1 (EFT1)   On December 5th, 2014, NASA flew the Orion Exploration Flight Test-1 (EFT-1), the first test flight of the Orion MPCV (now Artemis) Program[11]. It signaled the beginning of NASA's flagship program for exploration and aimed to stress Orion's heat shield from the high-speed entry velocities. Although the EFT-1 trajectory included two revolutions of the Earth with the second orbit being highly elliptical that brought the vehicle back at speeds comparable to a lunar return, the replicated profile for this study starts at EI and terminates off the coast near San Diego, CA as shown in Figure 3(b). Profiles using both APF and FNPEG are included where the scenario terminates at parachute deployment as illustrated in Figure 4(b). The initial conditions at EI and the targeted landing state for EFT-1 assumed for this study are provided in Table 2 and Table 4 respectively. The simulated EFT-1 nominal bank angle versus time, crossrange versus downrange, altitude versus velocity magnitude, and aero forces versus time profiles are shown for both APF and FNPEG in Figures 6(a), 6(b), 6(c), and 6(d) respectively. There are noticeable contrasts in each of these nominal performance metrics based on the selected entry guidance algorithm.

The Orion EFT-1 vehicle contained two Inertial Measurement Units (IMU), a Global Position System (GPS) receiver, two GPS antennas, and three Barometric Altimeters (BALT). The altimeter is only used for a backup navigation state and not used in the primary navigation filter. Although a star tracker is a baseline sensor for subsequent Orion Artemis missions, it was not included for the EFT-1 flight and not included in this scenario. During entry the extreme heat generated as the vehicle passes through the atmosphere produces a plasma wake that limits GPS measurement availability shortly after EI. During this GPS blackout period which has a duration of about 2-3 minutes, only gyro and accelerometer data is available to navigate Orion. As the vehicle reduces its speed from the atmospheric forces, GPS measurements eventually return[11].

C. Vehicle Configuration

For both the Mars and Earth entry scenarios, two different vehicle configurations are simulated for each. For Mars, the vehicle is modeled as MSL, as summarized in Table 5. For the Earth entry case, the Orion EFT-1 capsule configuration is simulated with the parameters provided in Table 6.

<table>
<tr><td colspan="2" align="center">Table 5   MSL vehicle modeling parameters</td></tr>
<tr><td>**Parameter**</td><td>**Value**</td></tr>
<tr><td>Initial Mass, kg</td><td>3300</td></tr>
<tr><td>Aeroshell Drop Mass, kg</td><td>1300</td></tr>
<tr><td>Aerodynamics</td><td>MSL-like spherecone</td></tr>
<tr><td>Reference Area, m^2</td><td>15.9</td></tr>
<tr><td>Thruster ISP, s</td><td>267</td></tr>
<tr><td>Thruster number</td><td>8</td></tr>
<tr><td>Thruster Max Thrust, N</td><td>3600 (Each)</td></tr>
</table>

<table>
<tr><td colspan="2" align="center">Table 6   Orion EFT-1 vehicle modeling parameters</td></tr>
<tr><td>**Parameter**</td><td>**Value**</td></tr>
<tr><td>Initial Mass, kg</td><td>10,177</td></tr>
<tr><td>Drop Mass, kg</td><td>NA</td></tr>
<tr><td>Aerodynamics</td><td>Orion-like spherecone</td></tr>
<tr><td>Reference Area, m^2</td><td>19.6</td></tr>
<tr><td>Thruster ISP, s</td><td>NA</td></tr>
<tr><td>Thruster number</td><td>NA</td></tr>
<tr><td>Thruster Max Thrust, N</td><td>NA</td></tr>
</table>

MSL Vehicle Configuration   The simulated MSL vehicle hits entry interface with a mass of 3300 kg with a 70-deg sphere-cone aerodynamic model and a reference area of 15.9 m^2, and flies at a nominal angle of attack of -10 degrees measured from the heatshield. At the end of entry guidance, the aeroshell is jettisoned, corresponding to a 1300 kg loss of mass to the vehicle. Eight thrusters are then ignited, with maximum thrust magnitudes of 3600 N each. The thrusters are modeled as one overall force on the vehicle, with an aggregate specific impulse (I_{SP}) of 267 s.

Orion EFT-1 Vehicle Configuration   The simulated Orion EFT-1 capsule reaches EI with a mass of 10,177 kg with a xx-deg sphere-cone aerdymic model and a reference area of 19.6 m^2.

III. GN&C Performance Analysis Modeling and Inputs
The GN&C performance analysis is based on the following modeling assumptions and input parameters regarding the entry guidance algorithms, navigation sensors, thruster actuators, environment modeling, and initial conditions at EI.

A. Entry Guidance Algorithms
Although during the entry, descent, and landing multiple guidance algorithms may be used for both atmospheric and powered flight, this section will only highlight the entry guidance algorithms that use atmospheric forces and torques to guide the vehicle toward the designated landing site. Details on the powered flight guidance algorithms if used are provided in [5]. The two different entry algorithms utilized for this study and demonstrated to highlight the impacts the selected strategy may have on the integrated GN&C performance. During the hypersonic entry segment of the trajectory, the vehicle uses the Apollo Final Phase (AFP) guidance algorithm or the Fully Numerical Predictor-Corrector Entry Guidance (FNPEG). These guidance strategies are used until heatshield jettison and powered descent initiation occur or when the parachutes are deployed.

Apollo Final Phase (AFP)   The AFP algorithm was chosen because it has extensive flight heritage, is relatively simple to implement, and has flight performance that is comparable with more complex algorithms. AFP is a terminal point controller which uses bank-angle lift modulation as depicted in Figure 7 to reduce terminal state errors. Errors are calculated during hypersonic entry relative to a pregenerated reference trajectory stored onboard the vehicle. The downrange error is controlled through the magnitude of the vertical component of the lift vector. Crossrange error is managed by performing bank reversals which flip the direction of the horizontal component of the lift vector and limit crossrange error growth.
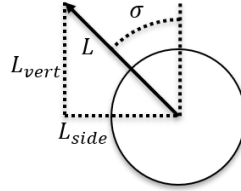

Fig. 7   Vertical and horizontal (side) lift components related to bank-angle steering.

The pregenerated reference trajectory is calculated by numerically integrating a three-degree-of-freedom model with a set bank-angle profile determined by mission designers. Control gains are then calculated by backwards-integrating the adjoint equations of motion. These gains, along with reference altitude-rate, aerodynamic acceleration, and range-to-go, are then stored onboard as a function of velocity. During flight, the vehicle compares the current navigated altitude-rate, acceleration, and range-to-go to the reference values in the stored table, and finds the required lift-to-drag ratio to null the final downrange error.

The commanded vertical lift-to-drag ratio ($L/D)_{cmd}$ is compared to the vehicle's nominal maximum vertical lift-to-drag capability ($L/D)_{nom}$, and this fraction is the cosine of the commanded bank angle, σ,

$$\sigma = \cos^{-1}\left(\frac{(L/D)_{cmd}}{(L/D)_{nom}}\right) \tag{8}$$

In the event of a commanded L/D being larger than the maximum L/D or smaller than the negative of the maximum, the commanded bank angle is saturated at 0 or 180 degrees, respectively. The calculation of $(L/D)_{cmd}$ is

$$\left(\frac{L}{D}\right)_{cmd} = \left(\frac{L}{D}\right)_{ref} + \frac{4(S_{act} - S_{pred})}{F_3} \tag{9}$$

where S_{act} is the actual range-to-go, and F_3 is a gain. The algorithm's predicted range-to-go, S_{pred}, is derived as

$$S_{pred} = S_{ref}(v) + F_2(v)(\dot{h} - \dot{h}_{ref}(v)) + F_1(v)(D - D_{ref}(v)) \tag{10}$$

where $S_{ref}(v)$ is the reference range-to-go based on the current velocity magnitude v, $F_2(v)$ and $F_3(v)$ are gains, $\dot{h}$ is the altitude rate, $\dot{h}_{ref}(v)$ is the reference altitude rate based on the current velocity, D is the aerodynamic drag acceleration, and $D_{ref}(v)$ is the reference aerodynamic drag acceleration based on the current velocity.

Fully Numerical Predictor-Corrector Entry Guidance (FNPEG)   As the name implies, FNPEG[9] is a numeric predictor-corrector (NPC) algorithm. Similar to AFP, FNPEG's output is a bank angle command. However, the core of FNPEG is management of a dimensionless *energy like* variable, e

$$e = \frac{1}{r} - \frac{v^2}{2} \tag{11}$$

where r is the vehicle's dimensionless radius magnitude and v is the vehicle's dimensionless velocity magnitude. The radius magnitude is normalized by the radius of the planet R_0, and the velocity is normalized by $V_{scale} = \sqrt{g_0 R_0}$, where g_0 is the planet's surface gravitational acceleration. The algorithm is attempting to bring the vehicle to a specified final altitude, velocity, and great-circle range to target, while avoiding exceeding prespecified maximum heat rate, aerodynamic acceleration, and dynamic pressure values.

The bank angle profile is parameterized by e as

$$|\sigma(e)| = \sigma_0 + \frac{e - e_0}{e_f - e_0}(\sigma_f - \sigma_0) \tag{12}$$

where σ is the bank angle, the subscript f denotes final conditions, and the subscript 0 denotes the value in the current predictor-corrector call. The predictor-corrector element is attempting to find a satisfactory value of σ_0 that will satisfy the terminal constraints. In FNPEG, this is done by attempting to minimize an error function

$$f(\sigma_0) = \frac{1}{2}[s(e_f) - s_f^*]^2 \tag{13}$$

where $s(e_f)$ is the estimated final range-to-go from the currently-estimated value of σ_0, and s_f^* is the final range-to-go requirement. This ends up taking the form of

$$\sigma_0^{(k+1)} = \sigma_0^k - \lambda_k \frac{z(\sigma_0^k)}{[z(\sigma_0^k - z(\sigma_0^{k-1})]}(\sigma_0^k - \sigma_0^{k-1}) \tag{14}$$

where λ is a step-size parameter and $z(\sigma_0)$ is the error function $s(e_f) - s_f^*$.

B. Navigation Sensors

Multiple types of navigation sensors are utilized during the different Mars and Earth EDL scenarios. The measurements processed onboard the vehicle could include the following: accelerometers, gyros, GPS, altimeter, velocimeter, and terrain relative navigation.

Accelerometer   The accelerometer measures the non-gravitational acceleration in the IMU case frame $\tilde{\mathbf{a}}^{imu}$, which is a function of the nominal inertial-to-body transformation matrix $\bar{\mathbf{T}}_i^b$, the nominal body-to-IMU transformation $\bar{\mathbf{T}}_b^{imu}$, the actual attitude dispersion $\boldsymbol{\theta}$, the misalignment $\boldsymbol{\mu}_a$, the constant scale factor $\mathbf{s}_a$, the Markov scale factor σ_a, the constant bias $\mathbf{b}_a$, the Markov bias $\boldsymbol{\beta}_a$, the nonorthogonality factor $\boldsymbol{\gamma}_a$, and the velocity random walk (noise) $\boldsymbol{\upsilon}_a$.

$$\tilde{\mathbf{a}}^{imu} = (\mathbf{I} + [(\mathbf{s}_a + \sigma_a)\searrow]) \left[(\mathbf{I} + [\boldsymbol{\mu}_a \times]) \, (\mathbf{I} + [\boldsymbol{\gamma}_a *]) \, \bar{\mathbf{T}}_b^{imu} \, (\mathbf{I} + [\boldsymbol{\theta} \times]) \, \bar{\mathbf{T}}_i^b \mathbf{a}^i + \mathbf{b}_a + \boldsymbol{\beta}_a + \boldsymbol{\upsilon}_a \right] \tag{15}$$

The uncertainty parameters used for the accelerometer are listed in Table 7.

Gyro   The gyros measure the vehicle's angular rates in the IMU case frame $\tilde{\omega}^{imu}$ and is represented as a function of the nominal body-to-IMU transformation $\bar{\mathbf{T}}_b^{imu}$ where b indicates the vehicle body-fixed frame, the misalignment $\boldsymbol{\mu}_\omega$, the constant scale factor $\mathbf{s}_\omega$, the Markov scale factor σ_ω, the constant bias $\mathbf{b}_\omega$, the Markov bias $\boldsymbol{\beta}_\omega$, the nonorthogonality factor $\boldsymbol{\gamma}_\omega$, and the angular random walk (noise) $\boldsymbol{\upsilon}_\omega$

$$\tilde{\omega}^{imu} = (\mathbf{I} + [(\mathbf{s}_\omega + \sigma_\omega)\diagdown]) \left[(\mathbf{I} + [\boldsymbol{\mu}_\omega\times]) \, (\mathbf{I} + [\boldsymbol{\gamma}_\omega*]) \, \bar{\mathbf{T}}_b^{imu}\omega^b + \mathbf{b}_\omega + \boldsymbol{\beta}_\omega + \boldsymbol{\upsilon}_\omega \right] \tag{16}$$

The uncertainty parameters used for the gyroscope are listed in Table 8.

Global Position System (GPS)   The vehicle is equipped with a GPS receiver to update the vehicle's inertial position and velocity. The simplified GPS sensor model perturbs the actual inertial position and velocity along with bias and noise terms

$$\tilde{\mathbf{r}}_c^i = \mathbf{r}_c + \mathbf{b}_{gps}^i + \boldsymbol{\beta}_{gps}^i + \boldsymbol{\eta}_{gps}^i \,, \tag{17}$$

The lander GPS error parameters are summarized in Table 10.

Altimeter   The altimeter has three beams separated by a specified angular distance where each beam provides a range measurement to the planet surface[12, 13]. The instrument is fixed in the body frame and measures the relative distance to the surface $\tilde{\rho}_{alt}$. The measurement is a function of the true surface range ρ, the scale factor s_{alt}, a bias b_{vel}, a Markov bias capturing the variations in the topography b_{ter}, and sensor noise v_{alt}.

$$\tilde{\rho}_{alt} = \rho \, (1 + s_{alt}) + b_{alt} + b_{ter} + v_{alt} \tag{18}$$

The true range between each beam's boresight and the surface can be expressed as a function of the vehicle's inertial-to-body transformation $\mathbf{T}_i^b$, the line-of-sight direction of the beam $\mathbf{u}_{beam}^b$, and the inertial position of the sensor mounted on the vehicle, $\mathbf{r}_{alt}^i$. This can be obtained by utilizing the following equality that relates the radius of the planet surface at the point of altimeter signal contact R_s with the vehicle's inertial position vector $\mathbf{r}^i$

$$R_s^2 = |\mathbf{r}_{alt}^i + \mathbf{T}_b^i \, \mathbf{u}_{beam}^b \rho|^2 \tag{19}$$

Expanding the above equation, gives

$$\rho^2 + 2\rho \left(\mathbf{T}_b^i \, \mathbf{i}_{alt}^b \right)^{\mathrm{T}} \mathbf{r}_{alt}^i + |\mathbf{r}_{alt}^i|^2 - R_s^2 = 0 \tag{20}$$

This quadratic polynomial in ρ can be used to solve for the true altimeter distance, ρ. The uncertainty parameters used for the altimeter are listed in Table 11.

Velocimeter   The velocimeter utilizes three beams generally aligned in a tetrahedron orientation to measure the relative velocity between the instrument and the planet surface. For each beam, the line-of-sight velocity or relative range-rate measurement to the surface $\tilde{v}_{vel}$ can be expressed as a function of the beam direction in the body frame $\mathbf{u}_{beam}^b$, the inertial-to-body transformation matrix $\mathbf{T}_i^b$, the inertial velocity of the velocimeter sensor $\mathbf{v}_{vel}^i$, the inertial position of the instrument $\mathbf{r}_{vel}^i$, the planets angular rate ω_p^i, a bias b_v, and measurement noise v_{vel}.

$$\tilde{v}_{vel} = \left(\mathbf{u}_{beam}^b \right)^T \mathbf{T}_i^b \left(\mathbf{v}_{vel}^i - \omega_p^i \times \mathbf{r}_{vel}^i \right) + b_v + v_{vel} \tag{21}$$

The uncertainty parameters used for the velocimeter are listed in Table 12.

Terrain Relative Navigation (TRN)   The TRN system generates a six degree-of-freedom position and orientation measurement relative to the surface. The measurement is modeled with a constant and a Markov bias. The relative position vector in the TRN frame is given by the equation

$$\tilde{\mathbf{r}}_{rel}^{trn} = \mathbf{T}_b^{trn}\mathbf{T}_i^b (\mathbf{r}_f - \mathbf{r}_l) + \mathbf{b}_\rho^{trn} + \boldsymbol{\beta}_\rho^{trn} + \boldsymbol{\eta}_\rho^{trn} \,, \tag{22}$$

where $\mathbf{r}_f$ is the preselected surface feature state and $\mathbf{r}_l$ is the lander inertial position vector, $\mathbf{b}_\rho^{trn}$ is the relative position constant bias, $\boldsymbol{\beta}_\rho^{trn}$ is the relative position Markov bias, and $\boldsymbol{\eta}_\rho^{trn}$ is the relative position measurement noise.

The relative attitude measurement in the TRN sensor frame is processed as a derived measurement, $\tilde{\theta}_{rel}^{trn}$. It is effectively the residual to be processed by the onboard navigation filter,

$$\mathbf{I} - \left[\tilde{\theta}_{rel}^{trn}\times\right] = \tilde{\mathbf{T}}_f^{trn}\left[\hat{\mathbf{T}}_i^f\hat{\mathbf{T}}_l^i\hat{\mathbf{T}}_{trn}^l\right] \tag{23}$$

where the estimate of the derived relative attitude measurement is a function of the target attitude uncertainty θ_f^f, the chaser attitude error state θ_l^l, the constant bias $\mathbf{b}_\theta^{trn}$, a Markov bias β_θ^{trn}, and noise η_θ^{trn}.

$$\tilde{\theta}_{rel}^{trn} = \hat{\mathbf{T}}_t^{trn}\theta_f^f - \hat{\mathbf{T}}_c^{trn}\theta_l^l + \mathbf{b}_\theta^{trn} + \beta_\theta^{trn} + \eta_\theta^{trn} \tag{24}$$

The uncertainty parameters used for the TRN are listed in Table 9.

Table 7   Accelerometer Uncertainty Parameters

Parameter	3-sigma value
Velocity Random Walk, $\mu g/\sqrt{Hz}$	150
Bias, μg	100
Scale Factor, ppm	175
Nonorthogonality, arcsec	15
Markov Bias, μg	15
Markov Scale Factor, ppm	175

Table 8   Gyroscope Uncertainty Parameters

Parameter	3-sigma value
Angular Random Walk, deg/$\sqrt{hr}$	0.018
Bias, deg/hr	0.15
Scale Factor, ppm	15
Nonorthogonality, arcsec	75
Markov Bias, deg/hr	0.09
Markov Scale Factor, ppm	15

Table 9   Terrain Relative Navigation Parameters [14]

Parameter	3-sigma value
Position Noise, m	15
Attitude Noise, deg	1.5
Position Bias, m	3
Attitude Bias, deg	0.1
Measurement Frequency, Hz	0.1

Table 10   GPS Uncertainty Parameters

Parameter	3-sigma value
Position Noise, m	15
Velocity Noise, m/s	1.5
Position Bias, m	3
Velocity Bias, m/s	0.1
Measurement Frequency, Hz	0.1

Table 11   Altimeter (NDL) Parameters [14]

Parameter	3-sigma value
Noise, m	6.6
Bias, m	1.5
Scale factor, %	0.1
Misalignment, arcsec	150
Min/Max Altitude	20 m / 6 km
Measurement Frequency, Hz	1

Table 12   Velocimeter (NDL) Parameters [14]

Parameter	3-sigma value
Noise, m/s	0.051
Bias, m/s	0.030
Scale Factor, %	0.25
Misalignment, arcsec	50
Max Vel/Altitude	200 m/s and 4 km
Measurement Frequency, Hz	1

C. Thruster Modeling

Only the MSL scenario assumes powered flight during the final descent phase of the EDL trajectory profile. Eight thrusters with a maximum thrust magnitude of 3600 N each are assumed. The thruster uncertainty parameters are shown in Table 13. For the Orion EFT-1 descent profile, parachutes are deployed and the vehicle is assumed to not do any active translational control following chute deployment as it gently drifts to the surface.

Table 13   MSL Thruster dispersions

Parameter	3-σ value
Bias, N	250
Scale Factor, nd	1×10^{-3}
Misalignment, deg	0.02
ISP Bias, s	10

D. Environment Modeling

Mars is modeled as a rotating spheroid with an inverse-square gravity field modified by J2 effects. The landing site is located at -4.0 km altitude relative to the spheroid. The atmosphere model used is the Mars Global Reference Atmospheric Model (GRAM) 2010, based on conditions anticipated during the flight profile of MSL. A lookup table was created from 1000 individual samples of Mars GRAM from an altitude of -4.5 km to 150 km. The model consists of nominal and standard deviation values for density and u, v, and w winds as functions of altitude. The nominal values are averaged from the samples, while standard deviations are calculated from the individual samples. Summary of the Mars environment model parameters are provided in Table 14.

Table 14   Simulated Mars Environment Parameters

Parameter	Value
Surface Model	Spheroid
Equatorial Radius, km	3396
Flattening Ratio, nd	0.00589
Rotation Rate, rad/s	7.09×10^{-5}
Atmosphere Model	Mars GRAM
Gravitational Parameter, m^3/s^2	4.289×10^{13}
J2 Perturbation, nd	1.96×10^{-3}

Table 15   Simulated Earth Environment Parameters

Parameter	Value
Surface Model	Spheroid
Equatorial Radius, km	3396
Flattening Ratio, nd	0.00589
Rotation Rate, rad/s	7.09×10^{-5}
Atmosphere Model	Earth GRAM
Gravitational Parameter, m^3/s^2	4.289×10^{13}
J2 Perturbation, nd	1.96×10^{-3}

E. Initial State Uncertainty at Entry Interface

At entry interface for both the Mars MSL vehicle and the Orion EFT-1 spacecraft, the uncertainty parameters associated with the initial trajectory dispersions, navigation errors, and process noise are summarized in Table 16 and Table 17.

Table 16   MSL dispersion sources and values.

MSL Parameter	3-σ value
EI Pos Dispersion, km	[1.0,1.0,1.0]
EI Vel Dispersions, m/s	[1.0,1.0,1.0]
EI Att Dispersions, deg	[0.3,0.2,0.25]
EI Att Rate, deg/s	[0.01,0.01,0.01]
EI Nav Pos Error, m	[21.1,53.1,19.4]
EI Nav Vel Error, m/s	[0.0275, 0.0234, 0.0258]
EI Nav Att Error, deg	1×10^{-4}
EI Nav Att Rate Error, deg/s	7×10^{-7}
Trans Process Noise, m/s/$\sqrt{s}$	1.2×10^{-3}
Rot Process Noise, rad/s/$\sqrt{s}$	1×10^{-6}

Table 17   Orion EFT-1 dispersion sources and values.

MSL Parameter	3-σ value
EI Pos Dispersion, km	[1.0,1.0,1.0]
EI Vel Dispersions, m/s	[1.0,1.0,1.0]
EI Att Dispersions, deg	[0.3,0.2,0.25]
EI Att Rate, deg/s	[0.01,0.01,0.01]
EI Nav Pos Error, m	[21.1,53.1,19.4]
EI Nav Vel Error, m/s	[0.02, 0.02, 0.02]
EI Nav Att Error, deg	1×10^{-4}
EI Nav Att Rate Error, deg/s	7×10^{-7}
Trans Process Noise, m/s/$\sqrt{s}$	1.2×10^{-3}
Rot Process Noise, rad/s/$\sqrt{s}$	1×10^{-6}

IV. GN&C Performance Analysis Trade Study Results

The integrated closed-loop GN&C analysis results include three major performance metric plots that include the trajectory dispersions, navigation errors, and propellant usage. These plots are generated and displayed for the following trades studies and comparison efforts that consist of the Mars MSL versus the Earth Orion EFT-1 EDL scenarios, APF versus FNPEG entry guidance algorithms, LinCov versus Monte Carlo analysis techniques. The trajectory dispersion plots shown in Figure 8 and Figure 9 highlight the dispersions in the following format: altitude versus velocity, altitude versus downrange, cross range versus downrange, and final position footprint dispersions. The navigation error plots displayed in Figure 10 and Figure 11 include the relative position navigation errors expressed in the inertial frame along with the body attitude errors. The total propellant usage for the MSL scenario is given in Figure 12 in terms of the expelled mass as well as the total accumulated delta-v. In general, the performance plots are organized such that the left column of sub-figures show the results when APF guidance is used during entry and the left column plots contains the results of the same performance metrics but when the FNPEG algorithm is utilized instead. A summary of the various trades and comparisons is ultimately provided in Table 18.

Table 18   Comparison of various nominal and dispersed values

Value	LinCov Nom	LinCov 3-σ	MC Nom	MC 3-σ	Nom+3-σ % Diff
Max Delta-V, m/s	496.87	48.92	496.87	50.41	0.27
Final Mass, kg	1654.31	28.89	1654.31	31.61	0.16
Dynamic Pressure, Pa	15837.35	1412.72	15837.00	1431.04	0.10
Touchdown Downrange, m	0.00	17.42	0.00	17.54	0.73
Touchdown Crossrange, m	0.01	14.72	0.01	14.87	1.00

Trajectory Dispersions   Trajectory dispersions serve as a direct performance metric of the integrated GN&C system performance and ultimately determines if a vehicle is able to achieve the critical mission objectives in a safe and precise manner. Details regarding the overall performance for the Mars MSL trajectory profile are given in Figure 8. Summarize and compare results in Figures 8(a), 8(c), 8(e), and , 8(g) for APF and Figure 8(b), 8(d), 8(f), and , 8(h)) for FNPEG. Similarly, the trajectory dispersions for the Orion EFT-1 profile is given in Figure 9. Summarize and compare results in Figures 9(a), 9(c), 9(e), and , 9(g) for APF and Figure 9(b), 9(d), 9(f), and , 9(h)) for FNPEG. Then draw any conclusions related to trajectory dispersions observed from results for both Mars and Earth scenarios.

Navigation Errors   The navigation system has a significant impacts on the entire GN&C system and often directly influences the overall trajectory dispersions. Ultimately the navigation errors determine how well the lander can estimate its current state (position, velocity, and attitude) to support the necessary EDL functions. Details regarding the overall navigation filter performance for the Mars MSL trajectory profile are given in Figure 10. Summarize and compare results in Figures 10(a) and 10(c) for APF and Figure 10(b) and 10(d) for FNPEG. Make note that there is very little discrepancy in the overall navigation errors between the two cases. Similarly, the navigation errors for the Orion EFT-1 profile is given in Figure 10. Summarize and compare results in Figures 11(a) and 11(a) for APF and Figure 11(b) and 11(d) for FNPEG. Then draw any conclusions related to trajectory dispersions observed from results for both Mars and Earth scenarios.

Propellant Usage   From a mission design perspective, propellant mass is a driving factor that heavily influences multiple facets of the mission. Understanding the expected propellant usage and the potential variations proves to be vital in maximizing mission objectives. Since only the MSL scenario demonstrates powered flight, the results are shown for this case in Figure 12. Summarize and compare results between Figures 12(a) and 12(c) for APF and Figures 12(b) and 12(d) for FNPEG. Make note that the propellant and delta-v usage for FNPEG is noticeably higher than APF. Comment why this is the case of the way these two scenarios are simulated. Note that the footprint dispersions for FNPEG are comparable to APF though the mass dispersions are significantly different. This is due to the large dispersions currently being observed with the FNPEG implementation between PDI and vertical descent.
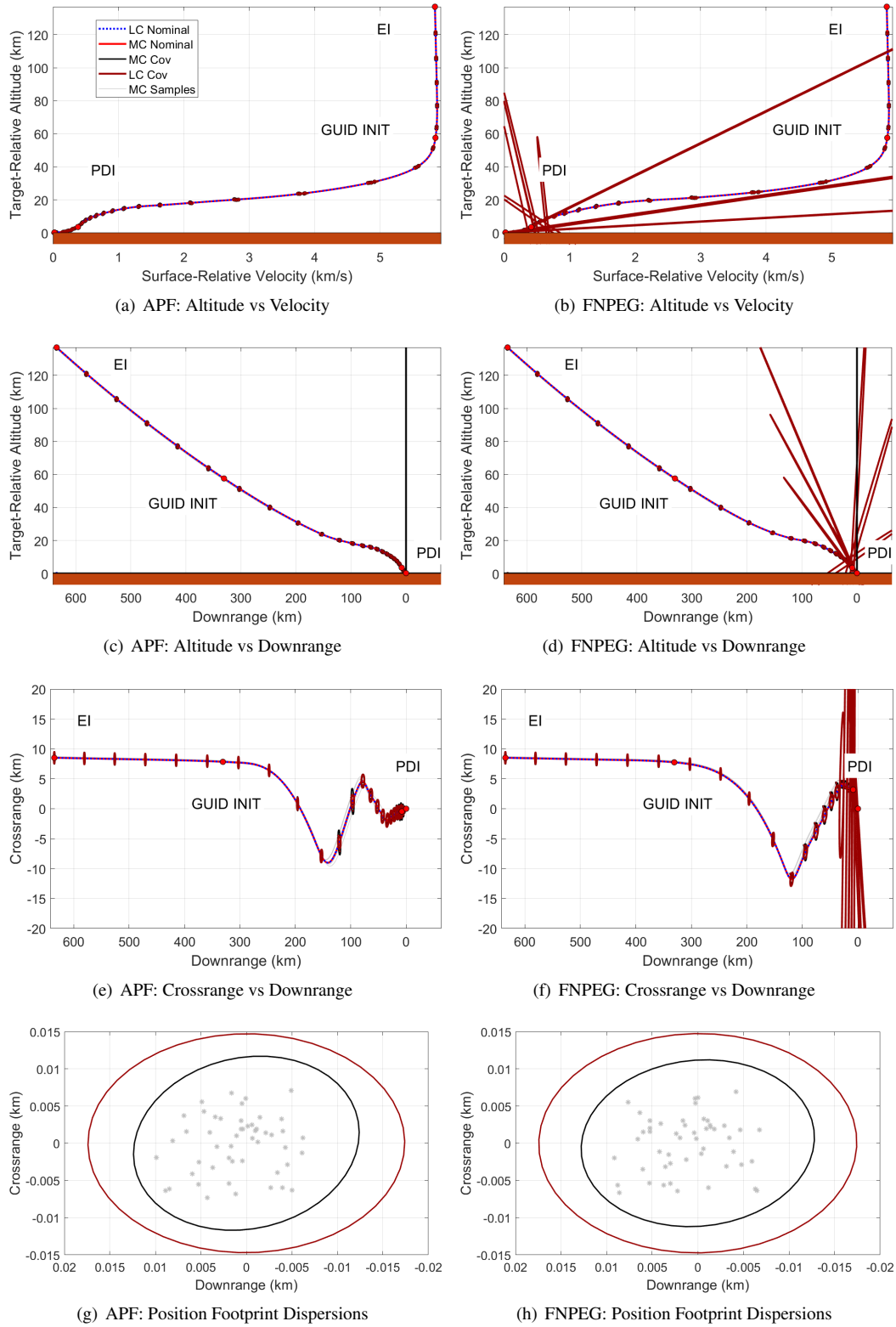
(a) APF: Altitude vs Velocity

(b) FNPEG: Altitude vs Velocity

(c) APF: Altitude vs Downrange

(d) FNPEG: Altitude vs Downrange

(e) APF: Crossrange vs Downrange

(f) FNPEG: Crossrange vs Downrange

(g) APF: Position Footprint Dispersions

(h) FNPEG: Position Footprint Dispersions

**Fig. 8   MSL Trajectory Dispersions using Apollo Final Phase (APF) and FNPEG**

(a) APF: Altitude vs Velocity

(b) FNPEG: Altitude vs Velocity

(c) APF: Altitude vs Downrange

(d) FNPEG: Altitude vs Downrange

(e) APF: Crossrange vs Downrange

(f) FNPEG: Crossrange vs Downrange

(g) APF: Position Footprint Dispersions

(h) FNPEG: Position Footprint Dispersions
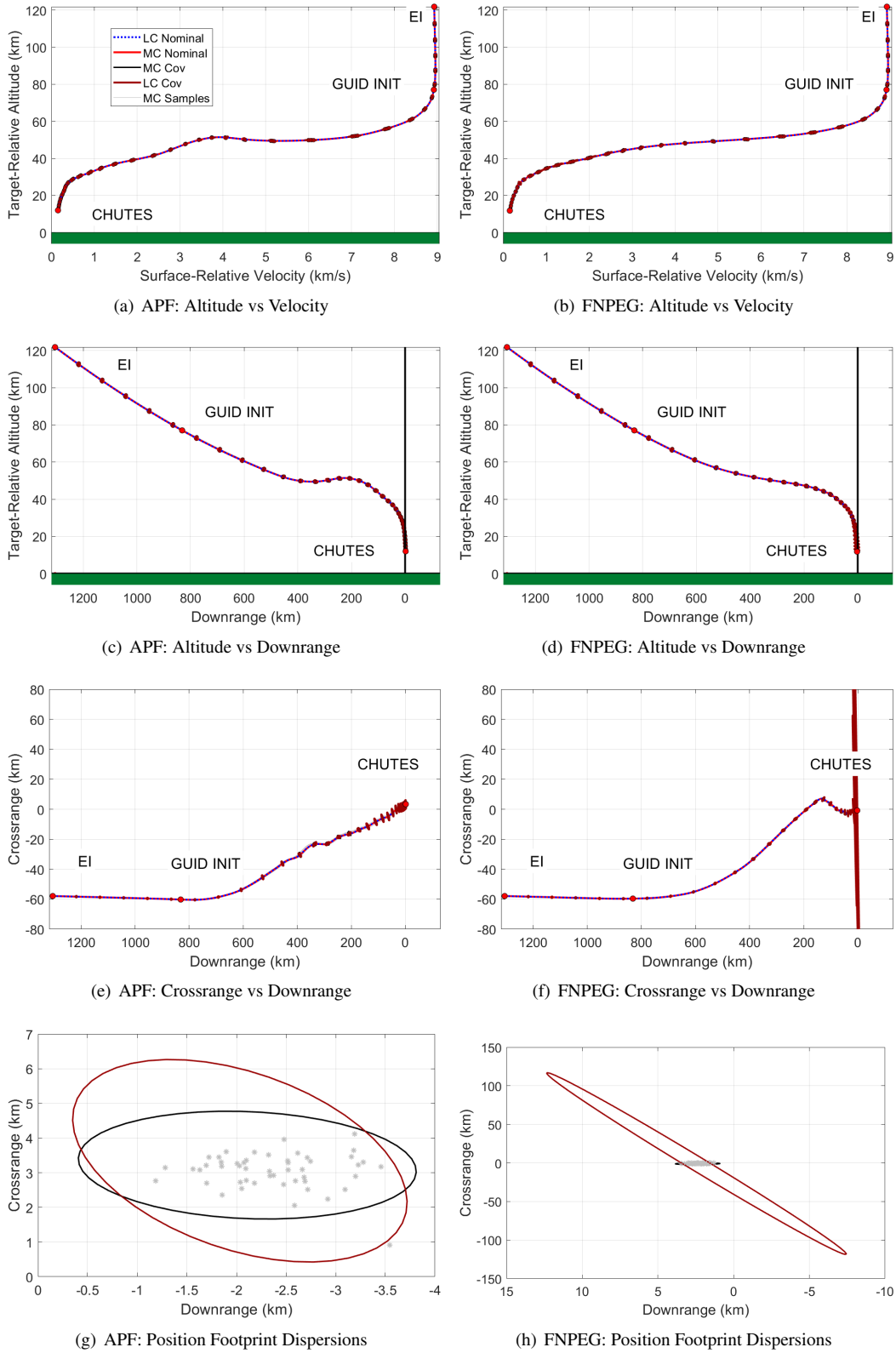
Fig. 9 Orion EFT-1 Trajectory Dispersions using Apollo Final Phase (APF) and FNPEG
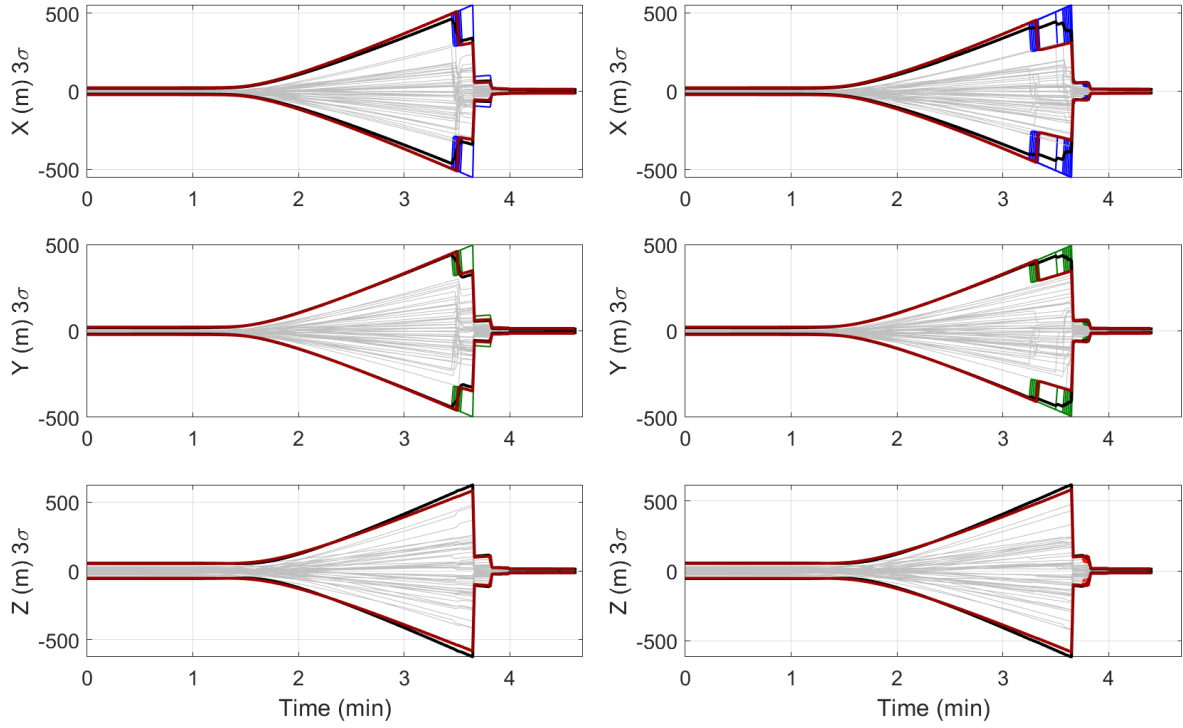
(a) APF Relative Position

(b) FNPEG Relative Position
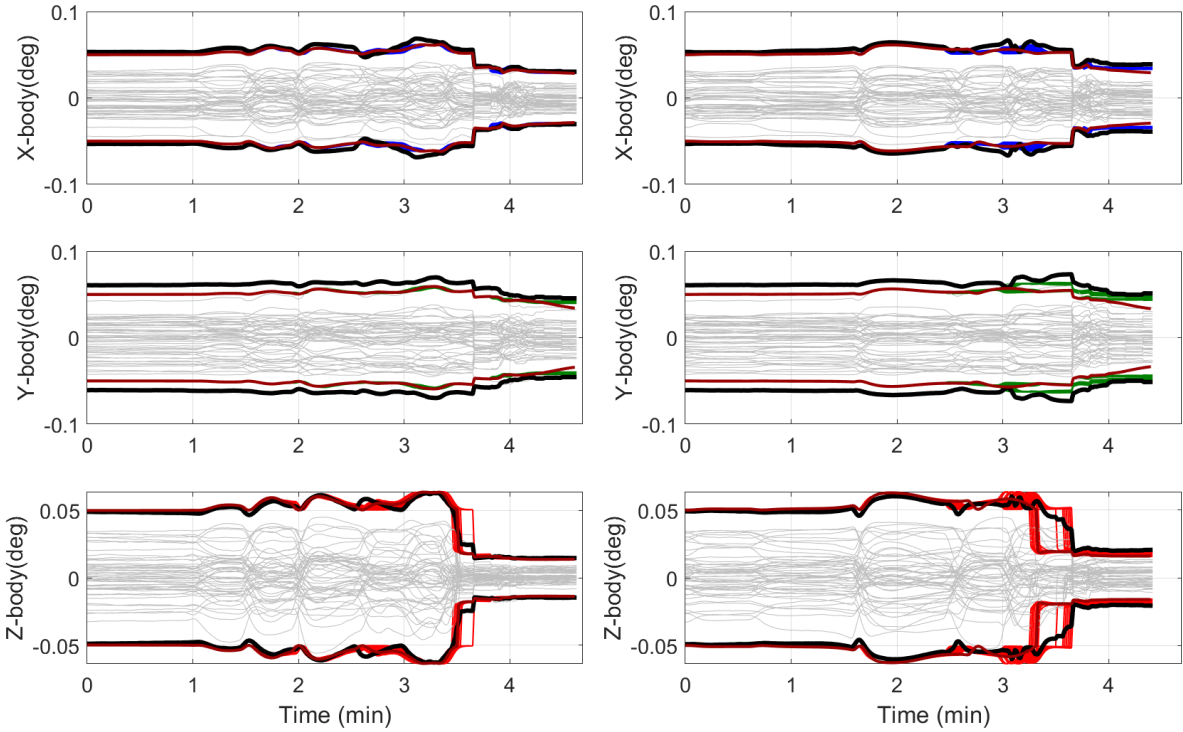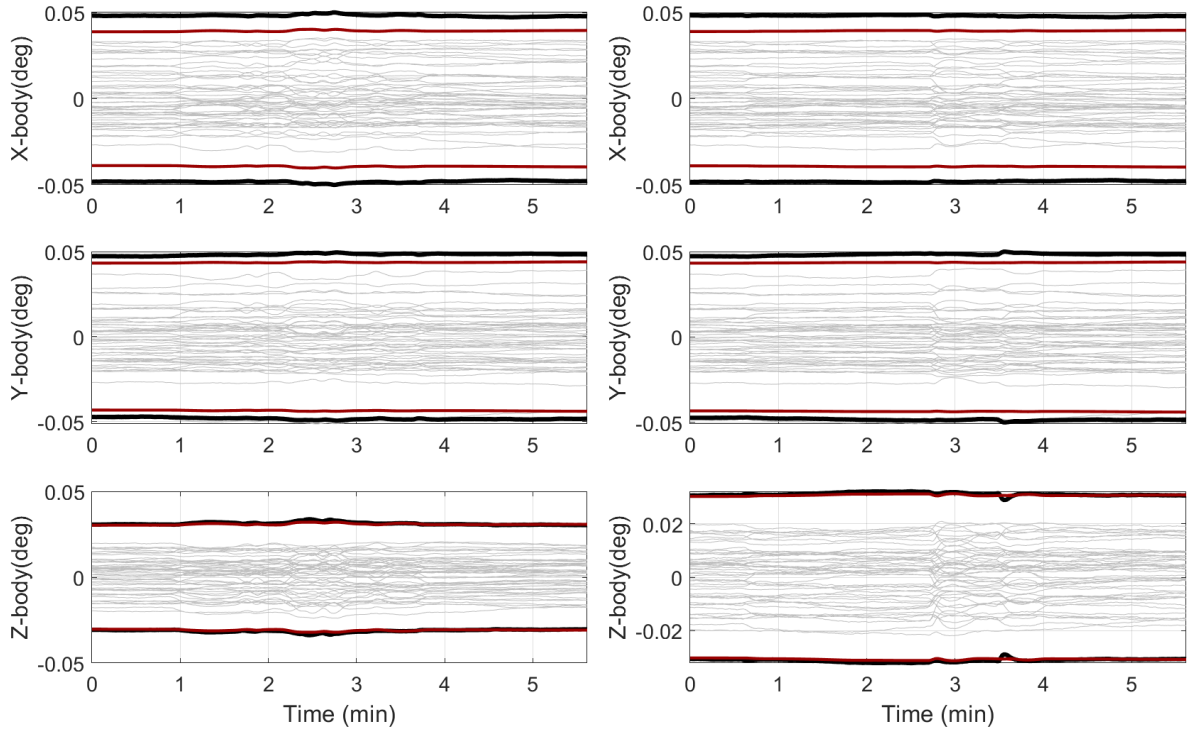
(c) APF Body Attitude

(d) FNPEG Body Attitude

Fig. 10   MSL Relative Navigation Errors Expressed in the Inertial Frame
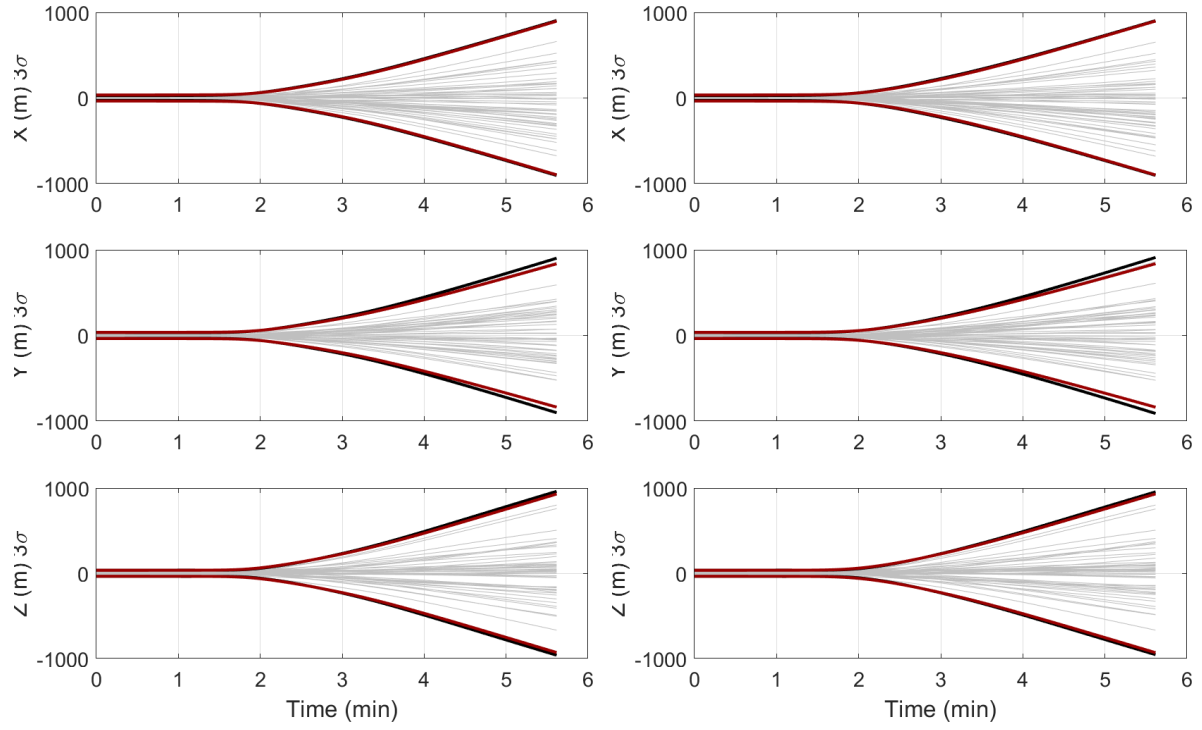
(a) APF Relative Position

(b) FNPEG Relative Position

(c) APF Body Attitude

(d) FNPEG Body Attitude

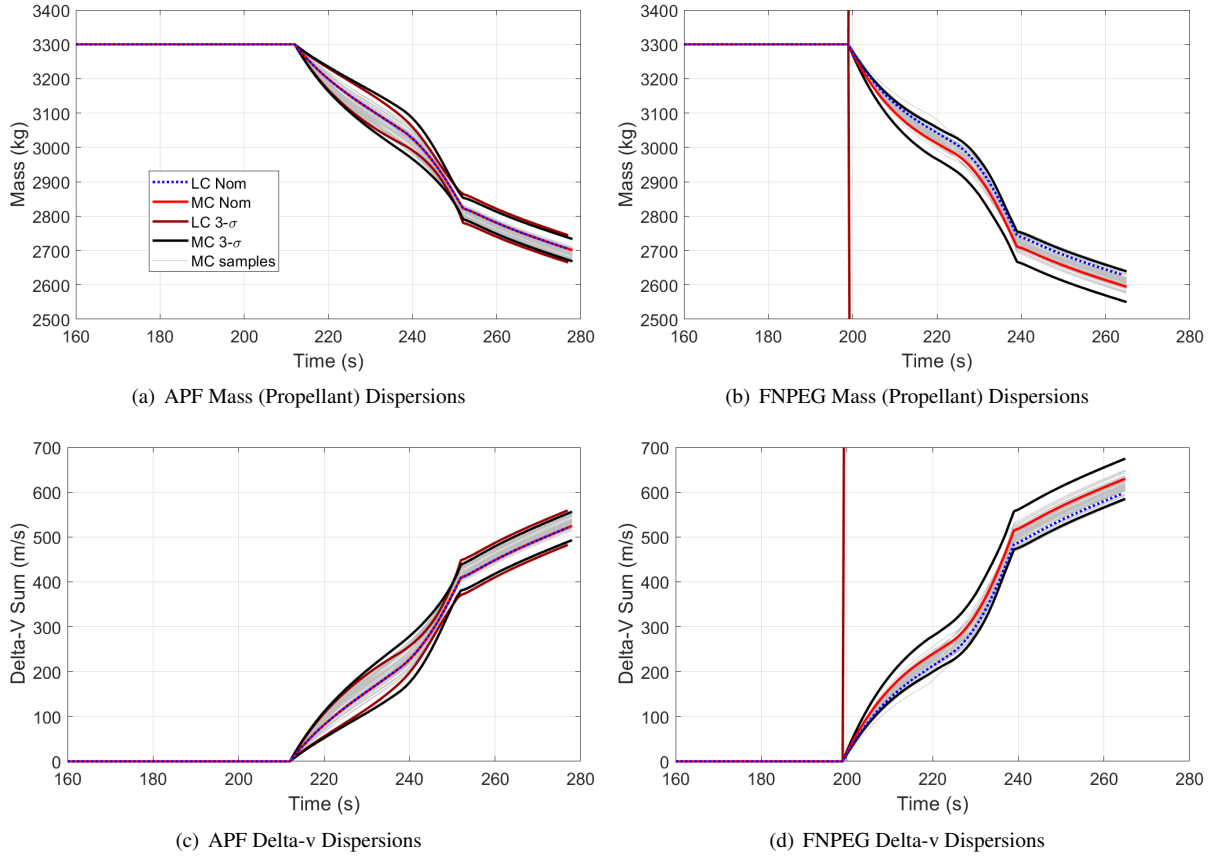**Fig. 11   EFT-1 Relative Navigation Errors Expressed in the Inertial Frame**

(a) APF Mass (Propellant) Dispersions

(b) FNPEG Mass (Propellant) Dispersions

(c) APF Delta-v Dispersions

(d) FNPEG Delta-v Dispersions

Fig. 12   Propellant and Delta-v Dispersion Metrics

Comparison Summary   A more quantitative comparison between several key performance metrics are highlighted in Table 18. While variations do exist between the calculated dispersions produced by LinCov and MC analysis techniques, they are typically within 2% of each other. Those these trends will vary at different epochs of flight, this helps highlight the basic concept that LinCov can be a viable complement to MC methods. Though MC methods provide a critical analysis capability for more high-fidelity studies and flight software development, testing and verification; linear covariance analysis can provide a rapid and reliable results for integrated GN&C systems. These LinCov results not only provide valuable insight at the early design phases of a project or program, they can provide a check to later analysis results produced using other techniques.

V. Conclusion

The SPLICE program continues to pursue the advancement of precision landing technology and to determine the flight hardware and GN&C algorithms that can achieve such an ambitious endeavor. To do so requires the ability to analyze a variety trade studies in a rapid and reliable manner such that requirements can be generated and system sensitivities can be identified early in the design process. One such technique that is emerging as a viable option for entry, descent, and landing is linear covariance analysis. Though Monte Carlo methods are the current standard and is ultimately the technique employed for formal verification and testing, LinCov can provide a complementary capability to support the conceptual and preliminary design phases of a program. Gaining understanding in utilizing linear covariance techniques in terms of its limitations and capabilities for atmospheric flight for EDL is crucial. This paper began to exercise and flex some of the recently validated capabilities of LinCov for 6-DOF atmospheric flight for multiple end-to-end scenarios, using multiple guidance algorithms, containing different sensor suites, applying multiple vehicle configurations, flying at different celestial bodies, and applying several analysis techniques. The speed and flexibility to evaluate the assortment of EDL conditions has been demonstrated.

Acknowledgments

References

[1] Sostaric, R. R., Pedrotty, S., Carson, J. M., Estes, J. N., Amzajerdian, F., Dwyer-Cianciolo, A. M., and Blair, J. B., "The SPLICE Project: Safe and Precise Landing Technology Development and Testing," *AIAA Scitech 2021 Forum*, 2021. https://doi.org/10.2514/6.2021-0256.

[2] Williams, J. W., Brandenburg, W. E., Woffinden, D. C., and Putnam, Z. R., "Validation of Linear Covariance Techniques for Mars Entry, Descent, and Landing Guidance and Navigaiton Performance Analysis," *AIAA Scitech 2022 Forum*, 2022. https://doi.org/10.2514/6.2020-0597.

[3] Jin, K., Geller, D., and Luo, J., "Development and Validation of Linear Covariance Analysis Tool for Atmospheric Entry," *Journal of Spacecraft and Rockets*, Vol. 56, No. 3, 2019, pp. 854–864. https://doi.org/10.2514/1.A34297.

[4] Woffinden, D., Robinson, S., Williams, J., and Putnam, Z. R., "Linear Covariance Analysis Techniques to Generate Navigation and Sensor Requirements for the Safe and Precise Landing Integrated Capabilities Evolution (SPLICE) Project," *AIAA Scitech 2019 Forum*, 2019. https://doi.org/10.2514/6.2019-0662.

[5] Williams, J., Woffinden, D., and Putnam, Z. R., "Mars Entry Guidance and Navigation Analysis Using Linear Covariance Techniques for the Safe and Precise Landing – Integrated Capabilities Evolution (SPLICE) Project," *AIAA Scitech 2020 Forum*, 2020. https://doi.org/10.2514/6.2020-0597.

[6] Markley, J., and Carpenter, J., "Generalized Linear Covariance Analysis," *The Journal of the Astronautical Sciences*, Vol. 57, No. 1-2, 2009, pp. 223–260. https://doi.org/10.1007/BF03321503.

[7] Luo, J., et al., "Robust Entry Guidance Using Linear Covariance-based Model Predictive Behavior," *International Journal of Advanced Robotic Systems*, Vol. 14, No. 1, 2017. https://doi.org/10.1177/1729881416687503.

[8] Dutta, S., and Braun, R. D., "Statistical Entry, Descent, and Landing Performance Reconstruction of the Mars Science Laboratory," *Journal of Spacecraft and Rockets*, Vol. 51, No. 4, 2014, pp. 1048–1061. https://doi.org/10.2514/1.A32937.

[9] Lu, P., "Entry Guidance: A Unified Method," *Journal of Guidance, Control, and Dynamics*, Vol. 37, No. 3, 2014, pp. 713–728. https://doi.org/10.2514/1.62605.

[10] D'Souza, C., and D'Souza, C., *An optimal guidance law for planetary landing*, 1997. https://doi.org/10.2514/6.1997-3709, URL https://arc.aiaa.org/doi/abs/10.2514/6.1997-3709.

[11] Gay, R. S., Holt, G. N., and Zanetti, R., "Orion Exploration Flight Test-1 Post-Flight Navigation Performance Assessment Relative to the Best Estimated Trajectory," *AAS 16-143*, ????

[12] Pierrottet, D. F., Amzajerdian, F., Petway, L. B., Hines, G. D., and Barnes, B., *Field Demonstration of a Precision Navigation Lidar System for Space Vehicles*, 2013. https://doi.org/10.2514/6.2013-4717.

[13] Pierrottet, D. F., Hines, G., Barnes, B., Amzajerdian, F., Petway, L., and Carson, J. M., *Navigation Doppler Lidar Integrated Testing Aboard Autonomous Rocket Powered Vehicles*, 2013. https://doi.org/10.2514/6.2018-0614.

[14] Dwyer-Cianciolo, A. M., Karlgaard, C. D., Woffinden, D., Lugo, R. A., Tynis, J., Sostaric, R. R., Striepe, S., Powell, R., and Carson, J. M., "Defining Navigation Requirements for Future Missions," *AIAA Scitech 2019 Forum*, ???? https://doi.org/10.2514/6.2019-0661.

[15] Zanetti, R., Woffinden, D., and Sievers, A., "Multiple Event Triggers in Linear Covariance Analysis for Spacecraft Rendezvous," *Journal of Guidance, Control, and Dynamics*, Vol. 35, No. 2, 2012, pp. 353–366. https://doi.org/10.2514/1.54965.